

Homogeneity in the early chemical evolution of the Sextans dwarf Spheroidal galaxy[★]

R. Lucchesi^{1,2,★★}, C. Lardo², F. Primas¹, P. Jablonka^{2,3}, P. North², G. Battaglia^{4,5}, E. Starkeburg⁶, V. Hill⁷, M. Irwin⁸, P. Francois³, M. Shetrone⁹, E. Tolstoy¹⁰, and K. Venn¹¹

¹ European Southern Observatory, Karl-Schwarzschild-str. 2, 85748 Garching bei München, Germany

² Physics Institute, Laboratoire d'astrophysique, École Polytechnique Fédérale de Lausanne (EPFL), Observatoire, 1290 Versoix, Switzerland

³ GEPI, Observatoire de Paris, CNRS, Université de Paris Diderot, 92195 Meudon Cedex, France

⁴ Instituto de Astrofísica de Canarias (IAC), Calle Via Láctea, s/n, 38205, San Cristóbal de la Laguna, Tenerife, Spain

⁵ Departamento de Astrofísica, Universidad de La Laguna, 38206, San Cristóbal de la Laguna, Tenerife, Spain

⁶ Leibniz-Institut für Astrophysik Potsdam, An der Sternwarte 16, D-14482 Potsdam, Germany

⁷ Laboratoire Lagrange, Université de Nice Sophia-Antipolis, Observatoire de la Côte d'Azur, France

⁸ Institute of Astronomy, University of Cambridge, Madingley Road, Cambridge CB3 0HA, U.K.

⁹ McDonald Observatory, University of Texas at Austin, Fort David, TX, USA

¹⁰ Kapteyn Astronomical Institute, University of Groningen, Landleven 12, NL-9747AD Groningen, the Netherlands

¹¹ Department of Physics and Astronomy, University of Victoria, PO Box 3055, STN CSC, Victoria BC V8W 3P6, Canada

Received ..., 2020; accepted ..., 2020

ABSTRACT

We present the high-resolution spectroscopic analysis of two new extremely metal-poor stars (EMPS) candidates in the dwarf spheroidal galaxy Sextans. These targets were pre-selected from medium resolution spectra centered around the Ca II triplet in the near-infrared and followed-up at higher resolution with VLT/UVES. We confirm their low metallicities with $[\text{Fe}/\text{H}]=-2.95$ and $[\text{Fe}/\text{H}]=-3.01$, placing them among the most metal-poor stars known in Sextans. The abundances of 18 elements, including C, Na, the α , Fe-peak, and neutron capture elements, are determined. In particular, we present the first measurements of Zn in a classical dwarf at extremely low metallicity. There has been previous hints of a large scatter in the abundance ratios of the Sextans stellar population around $[\text{Fe}/\text{H}]\sim -3$ when compared to other galaxies. We took the opportunity of this work to re-analyse the full sample of EMPS and find a Milky-Way-like plateau and a normal dispersion at fixed metallicity.

Key words. stars: abundances – Local Group – galaxies: dwarf – galaxies: formation

1. Introduction

In the cosmological Λ cold dark matter paradigm (Λ CDM), the assembly of large structures in the Universe arose from the coalescence of small systems and galaxy formation followed the cooling of the primordial gas in dark matter (DM) haloes (Press & Schechter 1974; White & Rees 1978; Springel et al. 2006). Dwarf spheroidal galaxies (dSphs) are most probably among the best representatives of the proto-galactic systems, given that they are the faintest and most DM-dominated galaxies known in the Universe. However, their exact significance and their role in galaxy formation are still to be clarified. In particular, the abundance patterns in dSph stars differ drastically from those of the field Milky Way (MW) halo population above $[\text{Fe}/\text{H}]\sim -2$ (Shetrone et al. 2001a; Venn et al. 2004a; Tolstoy et al. 2009; Letarte et al. 2010; Jablonka et al. 2015; Hill et al. 2019; Theiler et al. 2019). Nonetheless, dwarf galaxies offer the most metal-poor galactic environments that can be investigated. As such, their stellar populations provide crucial insights into the star formation conditions in the most pristine environments (e.g., Tolstoy et al. 2009; Frebel & Norris 2015).

Low-mass, long-lived extremely metal-poor (EMP, with $[\text{Fe}/\text{H}]\leq -3$) stars have kept the nucleosynthetic signatures of the first generation of stars in their atmospheres. Thus, by comparing the chemical patterns of these EMPS in galaxies of very different masses and star formation histories, from ultra-faint and classical dwarfs to the halo of the MW, one can directly test whether the primordial chemical evolution was a universal process and understand the relation between dwarfs and the building blocks of the more massive systems. Luckily, the proximity of a large number of Milky-Way satellites offers the unique opportunity to study the relevant aspects of their evolution in great detail and on a star-by-star basis.

The Sextans dSph was discovered by Irwin et al. (1990). At a distance of ~ 90 kpc, it is one of the closest satellite of the Milky Way (Mateo et al. 1995; Lee et al. 2003). It is very extended on the sky with a tidal radius of 120 ± 20 arcmin (Cicúendez et al. 2018) and low surface brightness $\sigma_0 = 18.2 \pm 0.5$ mag/arcmin² (Irwin & Hatzidimitriou 1995). It is a relatively low mass but strongly dark matter dominated classical dwarf spheroidal galaxy, $M/L \gg 100$, with a dynamical mass of about $3 \times 10^8 M_\odot$ measured out to a radius of ~ 3 kpc as seen in Fig. 6 of Breddels & Helmi (2013) (but see also Łokas (2009); Walker et al. (2010); Battaglia et al. (2011) for earlier measurements). The analysis of the colour-magnitude diagram (CMD) of Sex-

[★] Based on UVES observations collected at the ESO, proposal 093.D-0311.

^{★★} e-mail : romain.lucchesi@epfl.ch

tans reveals a stellar population which is largely dominated by stars older than ~ 11 Gyr (Lee et al. 2009; Bettinelli et al. 2018), with evidence for radial metallicity and age gradients, the oldest stars forming the most spatially extended component (Lee et al. 2003; Battaglia et al. 2011; Okamoto et al. 2017; Cicuéndez et al. 2018).

Very little is known on the metal-poor tail of the stellar population in Sextans, with only 8 EMPS so far followed-up at high resolution (Aoki et al. 2009; Tafelmeyer et al. 2010; Honda et al. 2011). The analysis of Aoki et al. (2009) suggested the possible existence of a set of low, sub-solar, $[\alpha/\text{Fe}]$ stars and an increased scatter at fixed metallicity compared to the Milky Way or even Sculptor (Starkenburg et al. 2013; Jablonka et al. 2015), which is nowadays the dSph with the largest number of studied EMPS. If confirmed this has strong implications for the formation processes of Sextans. Cicuéndez & Battaglia (2018) recently suggested that Sextans could have gone through an accretion/merger episode, this could explain the low $[\alpha/\text{Fe}]$ measurements of Aoki et al. (2009). But the most pressing need is nevertheless to increase the number of EMPS with detailed chemical abundances.

The ‘‘Dwarf Abundances and Radial velocity Team’’ (DART) formed around the ESO Large Program 171.B-0588(A) has surveyed Sextans up to its tidal radius with the medium resolution grism of FLAMES/GIRAFFE LR8 around the Ca II triplet (CaT). Starkenburg et al. (2010) provided the community with a metallicity calibration based on the CaT valid down to $[\text{Fe}/\text{H}] \sim -4$. This work enabled the identification of a set of new EMP candidates such as in Starkenburg et al. (2013); Jablonka et al. (2015) and the two targets of this study.

This paper is the first of a series targeting EMP candidates at high-resolution in Sextans, Fornax and Carina to probe the first stages of the chemical enrichment processes occurring in the early Universe. The paper is structured as follows: § 2 presents the observational material and data reduction. The determination of stellar parameters and the measurements of the elemental abundances along with their associated uncertainties are in § 3. Comments and remarks on the abundances of specific elements are provided in § 4. Finally we discuss our results and draw conclusions in § 5 and § 6.

2. Observations and data reduction

2.1. Target pre-selection, observations, and data reduction

The two EMP candidates of this work, S04–130 and S11–97, are red giant branch (RGB) stars that were selected from the CaT sample of Battaglia et al. (2011). The calibration of Starkenburg et al. (2013) led to low metallicity estimates $[\text{Fe}/\text{H}]_{\text{CaT}} < -2.8$.

S04–130 and S11–97 were followed-up at high resolution with the UVES spectrograph (Dekker et al. 2000) mounted at the ESO-VLT (program 093.D–0311(B)). We used the Dichroic1 mode with the gratings 390 Blue Arm CD#2 centered at 3900\AA and 580 Red Arm CD#3 centered at 5800\AA , together with a $1.2''$ slit, leading to a nominal resolution $R \sim 34,000$. The total wavelength coverage is $\sim 3200\text{--}6800\text{\AA}$ with effective usable spectral information starting from $\sim 3800\text{\AA}$. Each star has been observed for a total of 5 hours, split in 6 individual sub-exposures. The reduced data, including bias subtraction, flat fielding, wavelength calibration, spectral extraction, and order merging, were taken from the ESO Science Archive Facility.

Table 1 presents some details of the observations (spectral coverage, and signal to noise ratios per spectroscopic pixel) along with the coordinates of stars, their estimated metallicities

from the CaT calibration and measured heliocentric radial velocities (see § 2.2).

Figure 1 shows the colour-magnitude diagram (CMD) of Sextans probable members from Battaglia et al. (2011). Our UVES targets are highlighted in red. For comparison purposes, we also display the two EMPS, Sex24–72 and Sex11–04, that were observed with UVES and originally presented in Tafelmeyer et al. (2010) and the six EMPS (S10–14, S11–13, S11–37, S12–28, S14–98, and S15–19), which were observed with the high dispersion spectrograph installed on the 8.2m Subaru Telescope (Noguchi et al. 2002) and were discussed in Aoki et al. (2009). We refer to the original papers for additional details about the observations. We also show the spatial distribution of these EMPS.

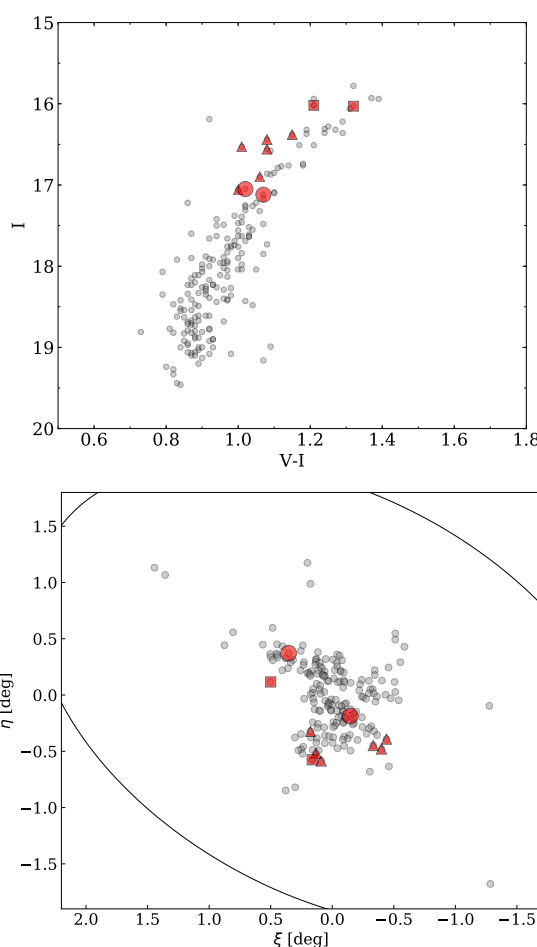


Fig. 1: The *top panel* displays the $V-I, I$ CMD of Sextans. Grey circles are Sextans probable members based on their $[\text{Fe}/\text{H}]_{\text{CaT}}$ metallicities and radial velocities (Battaglia et al. 2011). The red symbols refer to stars discussed in this paper. Large circles are the new targets of this work. The sample of Tafelmeyer et al. (2010) and Aoki et al. (2009) are shown with smaller squares and triangles, respectively. The *bottom panel* shows the spatial distribution of these stars. The ellipse indicates the tidal radius of Sextans.

Table 1: Journal of the observations. The blue and the red part of the spectra acquired with the 580 Red Arm CD#3 are considered separately. The λ range refers to the spectral ranges used in the analysis.

ID	$\alpha(J2000)$ [h:mn:s]	$\delta(J2000)$ [° :':"]	[Fe/H] _{CaT}	Setting [s]	λ range [Å]	S/N [/pix]	$\langle V_{rad, helio} \rangle$ [km s ⁻¹]
S04–130	10:14:28.02	-1:14:35.80	-2.89	Dic1-CD#2	3800–4520	15	214.76
				Dic1-CD#3(Blue)	4780–5750	45	215.56
				Dic1-CD#3(Red)	5830–6800	55	214.61
S11–97	10:12:27.89	-1:48:05.20	-2.80	Dic1-CD#2	3800–4520	16	218.06
				Dic1-CD#3(Blue)	4780–5750	52	218.63
				Dic1-CD#3(Red)	5830–6800	59	218.96

2.2. Radial velocities measurements

The heliocentric radial velocities (RVs) have been measured with the IRAF¹ task *rvidlines*, on each individual exposure. The final RV is the average of these individual values. This approach allows us to detect possible binary stars, at least those with RV variations detectable within almost one year². We did not find any evidence for binarity. Once corrected for RV shifts, the individual exposures were combined in a single exposure using the IRAF task *scombine* with sigma clipping. As a final step, each spectrum was visually examined and the few remaining cosmic rays were removed with the *splot* routine.

The average RV of each star (Table 1) coincides with the RV of Sextans ($226.0 \pm 0.6 \text{ kms}^{-1}$) within the velocity dispersion $\sigma = 8.4 \pm 0.4 \text{ kms}^{-1}$ measured by Battaglia et al. (2011), confirming that our stars are highly probable members.

3. Chemical analysis

3.1. Photometric temperature and gravity

The atmospheric parameters (APs) have been initially determined using photometric information. The first approximated determination of the stellar effective temperature was based on the V–I, V–J, V–H and V–K color indices measured by Battaglia et al. (2011) and J and Ks photometry taken from the VISTA commissioning data, which was also calibrated onto the 2MASS photometric system. We assumed $A_V = 3.24 \cdot E_{B-V}$ (Cardelli et al. 1989) and $E_{B-V} = 0.0477$ (Battaglia et al. 2011) for the reddening correction. The adopted photometric effective temperatures, T_{eff} , are listed in Table 2. They correspond to the simple average of the four colour-temperatures derived from V–I, V–J, V–H, V–K with the calibration of Ramírez & Meléndez (2005).

Because of the very small number of detectable Fe II lines in the very low metallicity regime, we determined the stellar surface gravity ($\log g$) from its relation with T_{eff} :

$$\log g_{\star} = \log g_{\odot} + \log \frac{M_{\star}}{M_{\odot}} + 4 \times \log \frac{T_{\text{eff}\star}}{T_{\text{eff}\odot}} + 0.4 \times (M_{\text{bol}\star} - M_{\text{bol}\odot})$$

assuming $\log g_{\odot} = 4.44$, $T_{\text{eff}\odot} = 5790 \text{ K}$, and $M_{\text{bol}\odot} = 4.75$ for the Sun. We adopted a stellar mass of $0.8 M_{\odot}$ and calculated the bolometric corrections using the Alonso et al. (1999) calibration and a distance of $d=90 \text{ kpc}$ (Karachentsev et al. 2004).

¹ Image Reduction and Analysis Facility; Astronomical Source Code Library ascl:9911.002

² Observations were performed between Apr,22 2015 and Jan, 29 2016.

3.2. Final stellar parameters and abundance determination

We determined the stellar chemical abundances through the measurement of the equivalent widths (EQWs) or the spectral synthesis of atomic transition lines, when necessary.

3.2.1. Linelist and model atmospheres

Our line list combines those of Jablonka et al. (2015), Tafelmeyer et al. (2010), and Van der Swaelmen et al. (2013). Information on the spectral lines is taken from the VALD database (Piskunov et al. 1995; Ryabchikova et al. 1997; Kupka et al. 1999, 2000). The central wavelengths and oscillator strengths are given in Table 3. The adopted solar abundances in Table 4 are from Asplund et al. (2009).

We adopted the new MARCS 1D atmosphere models, selecting the *Standard composition* class, i.e. including the classical α -enhancement of +0.4 dex at low metallicity. They were downloaded from the MARCS web site (Gustafsson et al. 2008), and interpolated using Thomas Masseron’s *interpol_modeles* code available on the same web site³. Inside a cube of 8 reference models, this code performs a linear interpolation on three given parameters : T_{eff} , $\log g$, and [Fe/H].

3.3. Abundances from EQWs and Spectral Synthesis

The EQWs were measured with DAOSPEC (Stetson & Pancino 2008). This code performs a Gaussian fit of each individual line and measures its corresponding EQW. Although DAOSPEC fits saturated Gaussians to strong lines, it can not fit the wider, Lorentz-like wings of the profile of very strong lines, in particular beyond 200 mÅ . This is especially relevant at very high resolution (Kirby & Cohen 2012). Therefore, for some of the strongest lines present in our spectra, we derived their abundances by spectral synthesis (see below).

The measured EQWs are provided in Table 3. Values in bracket indicate that the corresponding abundances were derived by spectral synthesis. The abundance derivation from EQWs and the spectral synthesis calculation were performed with the Turbospectrum code (Alvarez & Plez 1998; Plez 2012), which assumes local thermodynamic equilibrium (LTE), but treats continuum scattering in the source function. We used a plane parallel transfer for the line computation; this is consistent with our previous work on EMP stars (Tafelmeyer et al. 2010; Jablonka et al. 2015).

The stellar atmospheric parameters have been refined in an iterative manner. In order to constrain T_{eff} and the microturbulence velocities (v_t), we required no trend between the abun-

³ <http://marcs.astro.uu.se>

dances derived from Fe I and excitation potential (χ_{exc}) or the predicted⁴ EQWs (Magain 1984). Starting from the initial photometric parameters of Table 2, we adjusted T_{eff} and v_t by minimizing the slopes of the diagnostic plots allowing the slope to deviate from zero by no more than $\sim 2\sigma$, the uncertainties on the slopes. We did not force ionisation equilibrium between Fe I and Fe II taking into account that there will likely be effects of NLTE at these low metallicities (Mashonkina et al. 2017a). For each iteration the corresponding values of $\log g$ were computed from its relation with T_{eff} , assuming the updated values of T_{eff} , and adjusting the model metallicity to the mean iron abundance derived in the previous iteration.

We excluded from our analysis Fe I lines with $\chi_{exc} < 1.4$ eV, in order to minimize the impact of non-LTE on the measured abundances (Jablonka et al. 2015). Additionally, we used only the 580 setting data to calculate [Fe/H] and optimize the atmospheric parameters.

We derived the chemical abundances of the strong lines with measured EQW > 100 mÅ by spectral synthesis. These abundances have been obtained using our own code which performs a χ^2 -minimization between the observed spectral features and a grid of synthetic spectra calculated on the fly with Turbospectrum.

A line of a chemical element X is synthesized in a wavelength range of ~ 50 mÅ, the optimization is done by varying its abundance in steps of 0.1 dex, from $[X/\text{Fe}] = -1.0$ dex to $[X/\text{Fe}] = +1.0$ dex. In a same way, the resolution of the synthetic spectra is optimized, starting from the theoretical instrumental resolution, by convolving the spectra in large range of Gaussian widths for each abundance steps. A second optimization, with abundance steps of 0.01 dex is then performed, in a smaller range around the minimum χ^2 , in order to refine the results.

Similarly, the elements with a significant hyperfine structure (HFS) (namely, Sc, Mn, Co, and Ba) have been determined by running Turbospectrum in its spectral synthesis mode, in order to properly take into account blends and the HFS components in the abundance derivation (North et al. 2012).

The final (spectroscopic) parameters are given in Table 2. The typical uncertainties are ~ 100 K on T_{eff} , ~ 0.1 dex on $\log g$, assuming a $\pm 0.1 M_{\odot}$ error on M_{\odot} and a 0.2 mag error on M_{bol} , and about 0.15 km s^{-1} on v_t .

The final abundances reported in Table 4 are the average abundances from Table 3 based on EQWs or spectral synthesis, weighted by errors. For a few elements (V, Y and Zr) we were able to place only upper limits on their abundances (see Table 4). They are based on visual inspection of the observed spectrum, on which synthetic spectra were over-plotted with increasing abundances, until the χ^2 deviation became noticeable.

3.3.1. Error budget

1. *Uncertainties due to EQWs or spectral fitting* – The uncertainties on the EQW measurements (δ EQW) are estimated considering the errors provided by DAOSPEC (see Table 3) and computed according to the following formula (Stetson & Pancino 2008):

$$\delta EQW = \Delta \lambda^2 \sqrt{\sum_i (\delta I_i)^2 \left(\frac{\partial EQW}{\partial I_i}\right)^2 + \sum_i (\delta I_{C_i})^2 \left(\frac{\partial EQW}{\partial I_{C_i}}\right)^2}$$

where I_i and δI_i are the intensity of the observed line profile at pixel i and its uncertainty, while I_{C_i} and δI_{C_i} are the intensity and uncertainty of the corresponding continuum. The uncertainties on the intensities are estimated from the scatter of the residuals that remain after subtraction of the fitted line (or lines, in the case of blends). This is a lower limit to the real EQW error because systematic errors like the continuum placement are not accounted for. In order to account for additional sources of error, we added quadratically a 5% error to the EQW uncertainty, so that no EQW has an error smaller than 5%. This gives a mean uncertainty of $\sigma_{EQW} = 0.08$ rather than 0.04 in Fe I abundances. For the abundances derived by spectral synthesis (e.g. strong lines, hyperfine structure, or carbon from the G-band), the uncertainties were visually estimated by gradually changing the parameters of the synthesis until the deviation from the observed line became noticeable.

2. *Uncertainties due to the atmospheric parameters* – To estimate the sensitivity of the derived abundances to the adopted atmospheric parameters, we repeated the abundance analysis varying only one stellar atmospheric parameter at a time by its corresponding uncertainty, keeping the other ones fixed and repeating the analysis. The estimated internal errors are 100 K in T_{eff} , 0.1 dex in $\log(g)$, and 0.15 km s^{-1} in v_t . Table 5 lists the effects of those changes in the derived abundances for star S04–130. With comparable stellar parameters and SNR, the effects of changes of the atmospheric parameters on abundances are expected to be the same for star S11–97.

The final errors listed in Table 4 have been computed following the recipes outlined in Jablonka et al. (2015). The average abundance uncertainty due to the EQW error alone (σ_{EQW}) is computed as :

$$\sigma_{EQW} = \sqrt{\frac{N}{\sum_i 1/\sigma_i^2}},$$

where N represents the number of lines.

The σ_X errors correspond to the standard deviation of the individual line abundances :

$$\sigma_X = \sqrt{\frac{\sum_i (\epsilon_i - \bar{\epsilon})^2}{N - 1}},$$

where ϵ stands for the logarithmic abundance.

The final error on the average abundances is defined as $\sigma_{fin} = \max(\sigma_{EQW}, \sigma_X, \sigma_{Fe})$. As a consequence, no element X can have $\sigma_X < \sigma_{Fe}$; this is particularly important for species with a very small number of lines.

4. Specific comments on the abundance determination

In this part we comment on some specific behaviour among the absorption lines available in our spectra for a given element.

⁴ The use of observed EQWs would produce an increase of v_t by 0.1 – 0.2 km s^{-1} , which would reflect in a decrease of the measured [Fe/H] values by a few hundredths of a dex in a systematic way. Such a variation does not change the results in a significant way.

Table 2: Magnitudes, photometric and spectroscopic parameters are presented for the analyzed stars.

ID	<i>V</i>	<i>I</i>	<i>J</i>	<i>H</i>	<i>K</i>	Photometric Parameters					Final Parameters			
						<i>V</i> − <i>I</i>	<i>V</i> − <i>J</i>	<i>V</i> − <i>H</i>	<i>V</i> − <i>K</i>	mean	log(<i>g</i>) [cgs]	<i>T</i> _{eff} [K]	log(<i>g</i>) [cgs]	<i>v</i> _t [km s ^{−1}]
S04–130	18.071	17.050	16.162	15.543	15.418	4624	4735	4555	4567	4620	1.13	4520	1.07	1.70
S11–97	18.189	17.125	16.204	15.653	15.542	4543	4630	4549	4567	4572	1.15	4480	1.10	1.80

4.1. Carbon

The carbon abundance is determined from the intensity of the CH molecular band between 4323Å and 4324Å. Some of the carbon is locked in CO and CN molecules; as we are not able to measure the oxygen and nitrogen abundances, we assume that $[O/Fe] = [Mg/Fe]$ and that $[N/Fe]$ has a solar value, following Tafelmeyer et al. (2010) and Starkenburg et al. (2013). Synthetic spectra are then compared to the observed spectra. As an example, Figure 2 shows the comparison between the observed spectrum of S04–130 and five synthetic spectra computed with increasing carbon abundances.

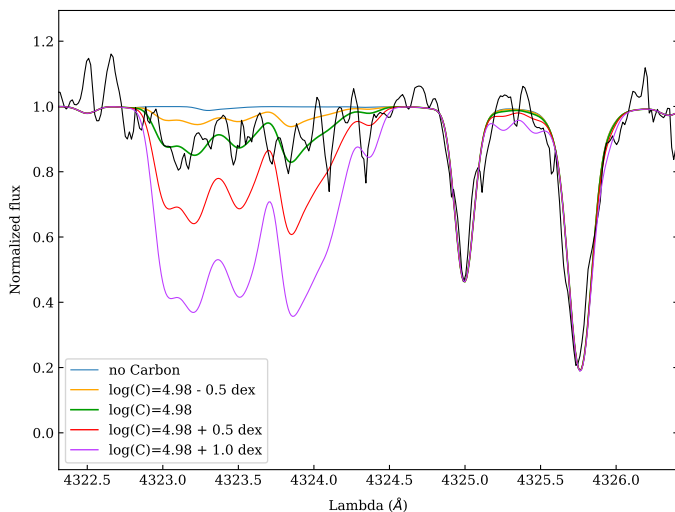


Fig. 2: From top to bottom, examples of synthetic spectra in the CH band are computed with increasing carbon abundances and over-plotted to the observed spectrum of S04–130 (black). The green third line represents our best representation of the data.

4.2. α elements

- *Magnesium*. The Mg abundance is based on 5 lines distributed from the violet to the yellow part of the spectrum. Four of them are rather strong, with EQW > 100 mÅ and non Gaussian line profiles. These lines yield abundances that are not consistent with the weaker line.

For this reason, we decided to derive the Mg abundance via spectral synthesis, which resulted in all lines giving consistent abundances. The EQW-based abundances derived for the weaker line is consistent with those obtained using spectral synthesis, confirming the validity of this method.

One more Mg I line is present in our spectra, at 44351 Å, but it was discarded because it is strongly blended with Fe, CH, and Cr I lines.

- *Silicon*. Two Si lines are detected in our spectra but they are in a noisy part of the spectrum and fall very close to the

strong Ca II absorption bands. The continuum level is hard to determine in this region, and the derived abundances strongly depend on it. Therefore, we did not derive any silicon abundance.

- *Titanium*. The Ti I abundances rely on 10–11 faint lines, all giving consistent abundance values. The Ti II abundances are based on 19–20 lines, they are slightly more scattered as many of them are rather strong. The mean abundances of Ti I and Ti II are different by $\Delta(Ti II - Ti I) = +0.26$ to $+0.29$ dex, this is explained by the fact that Ti II is less sensitive to NLTE effects than its neutral state. Thus, following Jablonka et al. (2015), for the purpose of our discussion we adopted the Ti II abundances as the most representative ones of the titanium content in our stars.

4.3. Iron-peak elements

- *Scandium*. The Sc abundance is based on 7 lines, they are all derived by spectral synthesis taking into account their HFS components. The smallest line (25mÅ) and the bluest line ($\lambda 4246.8$ Å) are both giving slightly larger abundances, while the other 4 lines are more consistent.
- *Chromium*. Cr relies on 7–9 lines, 4 are rather strong (EQW > 80mÅ), and the other 5 are weaker (EQW < 50m Å). Strong and weaker lines give more consistent results when abundances are determined through spectral synthesis. The $\lambda 5208$ Å line is blended with an Fe I line, and had therefore to be analysed via spectral synthesis.
- *Manganese*. All Mn lines (5) were synthesised taking into account their HFS components and they give consistent abundance results.
- *Cobalt*. Four lines are present in our spectra, they are all affected by hyperfine structure, and two of them ($\lambda 3894$ Å and $\lambda 3995$ Å) are blended with Fe I lines. Therefore, we derived all 4 lines abundances by spectral synthesis.
- *Nickel*. The Ni abundance is estimated from one or two strong lines and several very faint ones. Spectral synthesis gives consistent abundances for all lines.
- *Zinc*. There is only one line of zinc present in our observed spectra, at 4810 Å. The detection is clear but the line is faint, so the zinc abundance was derived via spectral synthesis.

4.4. Neutron capture elements

- *Strontium*. Two strong lines of strontium are detected in the blue part of our UVES spectra, but the abundances derived from their EQWs are quite discrepant (0.2 dex and 0.8 dex in our two stars, respectively). The 4215.5Å line of the star S11–97 is affected by the CN molecular band in this region. Spectral synthesis taking into account the carbon abundance derived in the CH band, led to an abundance more in agreement with the 4077.7Å line.

Table 3: Line parameters, observed equivalent widths, and elemental abundances. EQWs in brackets are given as indication only – for these lines the quoted abundances are derived via spectral synthesis.

El.	λ	χ_{ex}	$\log(gf)$	EQW [mÅ] S04–130	$\log\epsilon(X)$	EQW [mÅ] S11–97	$\log\epsilon(X)$	El.	λ	χ_{ex}	$\log(gf)$	EQW [mÅ] S04–130	$\log\epsilon(X)$	EQW [mÅ] S11–97	$\log\epsilon(X)$
C(CH)	4323				4.96		4.87	Mn I	4041.350	2.11	0.277	(38.2) ± (5.63)	2.22	(47.1) ± (5.88)	2.07
Na I	5889.951	0.00	0.108	(198.9) ± (16.26)	3.80	(189.1) ± (11.91)	3.79	Mn I	4823.520	2.32	0.121	(25.2) ± (2.52)	2.16	(27.3) ± (3.28)	2.06
Na I	5895.924	0.00	-0.194	(162.3) ± (9.93)	3.80	(179.2) ± (11.89)	3.79	Fe I	4859.741	2.88	-0.764	59.4 ± 4.97	4.56	– ± –	–
Mg I	3829.355	2.71	-0.227	– ± –	–	(176.0) ± (14.60)	5.09	Fe I	4871.318	2.87	-0.363	73.3 ± 5.55	4.43	74.8 ± 6.37	4.36
Mg I	3832.304	2.71	0.125	(190.7) ± (17.77)	5.13	– ± –	–	Fe I	4872.138	2.88	-0.567	58.8 ± 4.65	4.36	61.1 ± 5.83	4.33
Mg I	3838.294	2.72	-0.351	(214.5) ± (16.10)	5.13	(221.2) ± (18.00)	5.10	Fe I	4890.755	2.88	-0.394	78.2 ± 6.06	4.57	75.4 ± 5.62	4.42
Mg I	5172.684	2.71	-0.450	(131.3) ± (16.86)	5.10	(181.6) ± (14.09)	5.04	Fe I	4891.492	2.85	-0.112	83.3 ± 6.42	4.37	94.0 ± 7.37	4.48
Mg I	5183.604	2.72	-0.239	(146.8) ± (17.23)	5.11	(153.9) ± (15.23)	5.05	Fe I	4903.310	2.88	-0.926	52.6 ± 4.32	4.60	43.6 ± 3.52	4.37
Mg I	5528.405	4.35	-0.498	(59.8) ± (4.35)	5.08	(62.9) ± (4.67)	5.12	Fe I	4918.994	2.87	-0.342	78.0 ± 6.33	4.50	77.8 ± 6.03	4.39
Al I	3944.006	0.00	-0.623	(110.1) ± (20.41)	2.95	– ± –	–	Fe I	4920.502	2.83	0.068	93.5 ± 7.88	4.38	96.7 ± 7.49	4.33
Al I	3961.520	0.01	-0.323	(137.6) ± (11.71)	2.98	(138.4) ± (10.47)	3.05	Fe I	4924.770	2.28	-2.241	– ± –	–	28.4 ± 2.96	4.63
Si I	3905.523	1.91	-1.041	(185.6)	–	(195.4)	–	Fe I	4938.814	2.88	-1.077	32.7 ± 4.19	4.36	46.4 ± 4.36	4.56
Si I	4102.936	1.909	-3.140	(89.6)	–	(58.7)	–	Fe I	4939.687	0.86	-3.340	– ± –	–	76.0 ± 6.16	4.74*
Ca I	4283.011	1.89	-0.136	45.8 ± 4.48	3.42	49.1 ± 4.38	3.44	Fe I	4994.129	0.92	-3.080	63.0 ± 18.60	4.42*	– ± –	–
Ca I	4318.651	1.90	-0.139	41.7 ± 4.96	3.36	– ± –	–	Fe I	5006.119	2.83	-0.638	71.0 ± 6.02	4.59	72.6 ± 4.72	4.53
Ca I	4434.957	1.89	-0.007	– ± –	–	61.2 ± 6.60	3.51	Fe I	5041.072	0.96	-3.087	53.3 ± 19.70	4.30*	– ± –	–
Ca I	4454.779	1.90	0.258	79.4 ± 7.58	3.70	78.9 ± 6.43	3.61	Fe I	5041.756	1.49	-2.203	82.1 ± 6.99	4.66	89.3 ± 6.46	4.68
Ca I	5265.556	2.52	-0.113	– ± –	–	24.9 ± 2.67	3.64	Fe I	5049.820	2.28	-1.355	68.8 ± 5.09	4.54	69.1 ± 4.57	4.47
Ca I	5349.465	2.71	-0.310	– ± –	–	12.5 ± 1.62	3.69	Fe I	5051.634	0.92	-2.795	107.4 ± 8.62	5.03*	108.4 ± 8.49	4.88*
Ca I	5581.965	2.52	-0.555	11.1 ± 1.44	3.67	– ± –	–	Fe I	5068.766	2.94	-1.042	– ± –	–	37.3 ± 3.69	4.43
Ca I	5588.749	2.53	0.358	37.1 ± 3.23	3.44	40.5 ± 3.17	3.46	Fe I	5079.223	2.20	-2.067	43.3 ± 3.69	4.69	– ± –	–
Ca I	5857.451	2.93	0.240	– ± –	–	19.9 ± 2.15	3.63	Fe I	5079.740	0.99	-3.220	76.0 ± 6.07	4.89*	– ± –	–
Ca I	6102.723	1.88	-0.793	34.5 ± 3.12	3.71	33.2 ± 3.01	3.64	Fe I	5083.338	0.96	-2.958	88.7 ± 6.86	4.84*	91.2 ± 7.22	4.76*
Ca I	6122.217	1.89	-0.316	57.3 ± 4.71	3.63	59.7 ± 4.46	3.61	Fe I	5110.413	0.00	-3.760	116.9 ± 7.68	4.91*	117.3 ± 8.13	4.73*
Ca I	6162.173	1.90	-0.090	76.7 ± 5.84	3.75	75.5 ± 5.66	3.65	Fe I	5110.413	0.00	-3.760	81.7 ± 5.76	4.87*	77.6 ± 5.47	4.67*
Ca I	6439.075	2.53	0.390	47.8 ± 5.02	3.55	53.6 ± 4.20	3.60	Fe I	5127.359	0.92	-3.307	78.6 ± 5.17	4.92*	68.7 ± 5.02	4.62*
Sc II	4246.822	0.31	0.242	(128.0) ± (11.47)	0.33	(129.0) ± (8.83)	0.56	Fe I	5131.468	2.22	-2.515	21.1 ± 1.74	4.70	– ± –	–
Sc II	4314.083	0.62	-0.096	(93.2) ± (7.04)	0.32	(91.4) ± (7.92)	0.33	Fe I	5141.739	2.42	-1.964	23.9 ± 2.62	4.47	– ± –	–
Sc II	4400.389	0.61	-0.536	(73.8) ± (6.28)	0.48	(67.6) ± (5.93)	0.36	Fe I	5150.839	0.99	-3.003	75.2 ± 6.12	4.64*	74.4 ± 5.83	4.51*
Sc II	4415.557	0.60	-0.668	(82.7) ± (7.71)	0.50	(78.6) ± (8.43)	0.42	Fe I	5151.911	1.01	-3.322	63.1 ± 4.86	4.76*	63.1 ± 5.04	4.66*
Sc II	5031.021	1.36	-0.400	(31.5) ± (3.40)	0.20	(28.1) ± (6.15)	0.27	Fe I	5166.282	0.00	-4.195	97.1 ± 7.60	4.93*	91.2 ± 8.16	4.66*
Sc II	5526.790	1.77	0.024	(28.8) ± (3.31)	0.21	(28.2) ± (3.12)	0.18	Fe I	5171.596	1.49	-1.793	– ± –	–	108.0 ± 7.22	4.62
Sc II	5657.896	1.51	-0.603	(25.2) ± (2.69)	0.57	(25.3) ± (2.28)	0.49	Fe I	5191.455	3.04	-0.551	58.9 ± 4.77	4.50	56.4 ± 3.92	4.39
Ti I	3989.758	0.02	-0.130	65.8 ± 6.27	2.04	– ± –	–	Fe I	5192.344	3.00	-0.421	– ± –	–	62.7 ± 5.37	4.32
Ti I	3998.636	0.05	0.020	73.1 ± 10.27	2.10	72.6 ± 8.16	1.97	Fe I	5194.941	1.56	-2.090	81.6 ± 6.23	4.60	91.7 ± 5.73	4.68
Ti I	4981.730	0.85	0.570	58.2 ± 4.79	2.06	59.3 ± 5.36	1.99	Fe I	5198.711	2.22	-2.135	37.1 ± 3.49	4.66	– ± –	–
Ti I	4991.066	0.84	0.450	47.4 ± 5.44	1.97	51.9 ± 3.51	1.97	Fe I	5202.336	2.18	-1.838	60.3 ± 4.47	4.72	56.5 ± 4.92	4.57
Ti I	4999.503	0.83	0.320	37.7 ± 3.67	1.91	41.9 ± 3.54	1.92	Fe I	5216.274	1.61	-2.150	84.6 ± 5.75	4.78	83.7 ± 6.88	4.64
Ti I	5014.276	0.81	0.040	34.6 ± 4.25	2.12	43.2 ± 5.68	2.20	Fe I	5217.389	3.21	-1.070	29.3 ± 2.59	4.68	21.9 ± 1.92	4.46
Ti I	5039.958	0.02	-1.080	26.7 ± 2.56	2.06	26.7 ± 3.42	1.98	Fe I	5225.526	0.11	-4.789	54.2 ± 4.73	4.88*	55.5 ± 4.21	4.79*
Ti I	5064.653	0.05	-0.940	30.1 ± 2.94	2.02	29.5 ± 2.71	1.93	Fe I	5232.940	2.94	-0.058	– ± –	–	93.5 ± 6.97	4.46
Ti I	5173.743	0.00	-1.060	29.7 ± 2.90	2.06	31.9 ± 3.25	2.03	Fe I	5254.956	0.11	-4.764	57.2 ± 4.70	4.90*	55.7 ± 4.88	4.77*
Ti I	5192.969	0.02	-0.950	33.7 ± 2.59	2.06	25.7 ± 2.96	1.81	Fe I	5266.555	3.00	-0.386	70.4 ± 4.67	4.50	63.8 ± 5.03	4.29
Ti I	5210.384	0.05	-0.820	37.5 ± 3.24	2.03	38.1 ± 3.01	1.96	Fe I	5269.537	0.86	-1.321	168.6 ± 13.44	4.60*	162.3 ± 12.88	4.29*
Ti II	3913.461	1.12	-0.360	111.3 ± 10.96	2.23	130.4 ± 10.47	2.54	Fe I	5281.790	3.04	-0.834	45.6 ± 3.51	4.53	– ± –	–
Ti II	4028.338	1.89	-0.920	51.8 ± 5.28	2.27	– ± –	–	Fe I	5302.300	3.28	-0.720	40.6 ± 3.75	4.63	33.0 ± 2.55	4.43
Ti II	4290.215	1.16	-0.870	101.5 ± 10.88	2.37	96.1 ± 9.15	2.16	Fe I	5307.361	1.61	-2.987	– ± –	–	36.5 ± 3.14	4.64
Ti II	4337.914	1.08	-0.960	– ± –	–	88.6 ± 9.87	1.96	Fe I	5324.179	3.21	-0.103	67.9 ± 5.54	4.43	69.3 ± 5.82	4.37
Ti II	4394.059	1.22	-1.770	57.1 ± 6.02	2.31	55.2 ± 5.11	2.24	Fe I	5328.039	0.92	-1.466	157.6 ± 12.17	4.60*	165.1 ± 12.79	4.53*
Ti II	4395.031	1.08	-0.540	119.8 ± 11.33	2.34	120.5 ± 8.98	2.26	Fe I	5332.899	1.56	-2.777	51.7 ± 4.46	4.70	44.6 ± 3.67	4.50
Ti II	4395.839	1.24	-1.930	55.9 ± 5.67	2.48	46.0 ± 5.41	2.26	Fe I	5367.466	4.41	0.443	20.4 ± 2.25	4.42	– ± –	–
Ti II	4399.765	1.24	-1.200	89.2 ± 8.73	2.46	89.0 ± 8.65	2.38	Fe I	5369.961	4.37	0.536	31.5 ± 3.28	4.54	30.3 ± 2.74	4.47
Ti II	4417.713	1.16	-1.190	96.6 ± 8.29	2.54	97.1 ± 8.85	2.47	Fe I	5371.489	0.96	-1.645	152.3 ± 10.99	4.72*	148.0 ± 11.19	4.44*
Ti II	4443.801	1.08	-0.710	103.7 ± 8.14	2.11	112.6 ± 7.36	2.23	Fe I	5383.369	4.31	0.645	37.2 ± 2.63	4.47	– ± –	–
Ti II	4444.554	1.12	-2.200	– ± –	–	44.5 ± 4.80	2.34	Fe I	5393.167	3.24	-0.715	36.3 ± 3.08	4.49	– ± –	–
Ti II	4450.482	1.08	-1.520	82.1 ± 7.47	2.41	80.9 ± 8.77	2.32	Fe I	5397.128	0.92	-1.993	137.9 ± 9.29	4.72*	140.7 ± 9.57	4.59*
Ti II	4464.449	1.16	-1.810	– ± –	–	59.0 ± 7.16	2.27	Fe I	5405.774	0.99	-1.844	143.0 ± 10.31	4.77*	144.3 ± 9.38	4.60*
Ti II	4468.493	1.13	-0.630	95.2 ± 7.28	1.89	– ± –	–	Fe I	5410.910	4.47	0.398	– ± –	–	22.3 ± 2.41	4.55
Ti II	4501.270	1.12	-0.770	116.2 ± 12.60	2.48	– ± –	–	Fe I	5424.068	4.32	0.520	– ± –	–	34.1 ± 3.15	4.50
Ti II	4865.610	1.12	-2.700	– ± –	–	25.9 ± 3.79	2.43	Fe I	5429.696	0.96	-1.879	149.9 ± 10.72	4.88*	148.3 ± 11.05	4.66*
Ti II	5129.156	1.89	-1.340	36.0 ± 3.96	2.25	34.0 ± 2.86	2.20	Fe I	5434.523	1.01	-2.122	129.9 ± 9.27	4.81*	127.5 ± 9.19	4.59*
Ti II	5154.068	1.57	-1.750	31.4 ± 2.58	2.16	35.5 ± 3.33	2.22	Fe I	5446.917	0.99	-1.914	140.1 ± 10.22	4.77*	139.6 ± 11.11	4.57*
Ti II	5185.902	1.89	-1.410	33.1 ± 3.41	2.26	29.8 ± 2.76	2.18	Fe I	5455.609						

Table 3: continued.

El.	λ	χ_{ex}	$\log(gf)$	EQW [mÅ] S04–130	$\log\epsilon(X)$	EQW [mÅ] S11–97	$\log\epsilon(X)$
Fe I	6494.980	2.40	-1.273	82.4 ± 6.50	4.69	82.9 ± 5.47	4.60
Fe I	6592.913	2.73	-1.473	– ± –	–	37.1 ± 2.91	4.46
Fe I	6677.985	2.69	-1.418	52.0 ± 3.82	4.67	51.9 ± 3.86	4.60
Fe II	4923.921	2.89	-1.320	105.3 ± 8.38	4.84	77.4 ± 20.37	4.19
Fe II	5018.436	2.89	-1.220	112.8 ± 9.03	4.87	82.2 ± 18.06	4.17
Fe II	5197.567	3.23	-2.100	– ± –	–	32.9 ± 3.04	4.52
Fe II	5234.623	3.22	-2.230	42.2 ± 3.06	4.82	– ± –	–
Fe II	5275.997	3.20	-1.940	50.1 ± 4.83	4.65	54.6 ± 5.04	4.72
Fe II	5284.103	2.89	-2.990	24.3 ± 2.28	4.80	– ± –	–
Co I	3845.468	0.92	0.010	(71.7) ± (6.95)	2.12	(76.5) ± (7.96)	1.75
Co I	3894.077	1.05	0.100	(95.1) ± (9.97)	2.19	(105.7) ± (11.03)	1.74
Co I	3995.307	0.92	-0.220	(73.3) ± (7.88)	1.92	(80.2) ± (6.01)	1.80
Co I	4121.318	0.92	-0.320	(92.0) ± (8.20)	1.96	(76.7) ± (6.59)	1.82
Ni I	3858.297	0.42	-0.960	(116.3) ± (9.28)	3.44	– ± –	–
Ni I	5084.096	3.68	0.030	– ± –	–	(11.4) ± (2.06)	3.34
Ni I	5155.764	3.90	0.074	– ± –	–	(10.4) ± (1.50)	3.46
Ni I	5476.904	1.83	-0.780	(55.9) ± (18.23)	3.21	(76.2) ± (5.51)	3.13
Ni I	6643.630	1.68	-2.220	(20.7) ± (2.04)	3.33	– ± –	–
Ni I	6767.772	1.83	-2.140	(24.9) ± (2.58)	3.60	(19.1) ± (3.25)	3.54
Zn I	4810.528	4.08	-0.137	(29.1) ± (3.69)	2.25	(23.0) ± (2.92)	2.10
Sr II	4077.709	0.00	0.167	(144.5) ± (12.00)	0.17	(81.6) ± (15.38)	-0.60
Sr II	4215.519	0.00	-0.145	(122.0) ± (9.62)	-0.02	(132.1) ± (13.51)	-0.35
Y II	4883.682	1.08	0.070	(13.2) ± (2.02)	-1.20	(14.9) ± (2.36)	-1.33
Y II	5200.410	0.99	-0.570	– ± –	–	(12.0) ± (1.50)	-1.01
Y II	5205.722	1.03	-0.340	(11.7) ± (2.15)	-1.12	– ± –	–
Zr II	4208.980	0.71	-0.510	(24.2) ± (3.56)	-0.25	(30.1) ± (3.13)	-0.39
Ba II	4934.076	0.00	-0.150	(89.6) ± (7.38)	-1.59	(92.6) ± (8.39)	-1.62
Ba II	5853.668	0.60	-1.000	(13.3) ± (1.42)	-1.46	– ± –	–
Ba II	6141.713	0.70	-0.076	(42.1) ± (3.95)	-1.64	(44.8) ± (3.33)	-1.65
Ba II	6496.897	0.60	-0.377	(39.2) ± (3.31)	-1.53	(38.4) ± (3.44)	-1.57
Pr II	4143.112	0.37	0.609	– ± –	–	14.6 ± 4.29	-1.82
Nd II	4446.380	0.20	-0.350	15.1 ± 4.46	-1.12	– ± –	–

- *Yttrium*. Two very faint lines (<15 mÅ) of yttrium could be detected in our spectra, but we were able to place only upper limits on the Y abundance in our stars.
- *Barium*. Four lines of barium are present in our wavelength ranges. One is very faint ($\lambda 5853$ Å) and detected for only one star, while the other three lines are strong, with two of them blended with weak iron lines ($\lambda 4934$ Å and $\lambda 6141$ Å). Therefore, we proceeded by spectral synthesis, taking into account all blends and the Ba HFS components. Barium has five isotopes; the fraction of even-A and odd-A (A=atomic mass) nuclei ($^{134}\text{Ba} + ^{136}\text{Ba} + ^{138}\text{Ba}$) : ($^{135}\text{Ba} + ^{137}\text{Ba}$) was fixed to 82:18, following Jablonka et al. (2015). The spectrum syntheses yielded consistent abundances for the 3-to-4 Ba lines.

5. Discussion

5.1. Carbon

Figure 3 shows that none of our stars can be considered as carbon-enhanced using the Aoki et al. (2007) criterion. Nonetheless, our stars are evolved enough to have converted C into N by the CNO cycle, as they are above $\log(L_*/L_\odot) = 2.3$, i.e. the limit above which a metal-poor $0.8 M_\odot$ star is thought to undergo extra-mixing between the bottom of the stellar convective envelope and the outer layer of the advancing hydrogen-shell (see Placco et al. 2014, and references therein for a discussion). Placco et al. (2014) developed a procedure to correct the measured carbon abundances based on stellar-models evolution and depending on the $\log(g)$ of the stars. They have shown that applying these corrections to their dataset, the fraction of carbon-rich stars $[C/Fe] > +0.7$ increased to 43% for $[Fe/H] < -3$. The corrections are interpolated⁵ at given $\log(g)$, $[Fe/H]$ and $[C/Fe]$. For the star S04–130, the corresponding correction is +0.73 dex,

⁵ <https://vplacco.pythonanywhere.com/>

resulting in a ratio of $[C/Fe] = 0.20$ dex. For S11–97 the derived correction is +0.74 dex, resulting in $[C/Fe] = 0.19$ dex and keeping the two stars right under the limit of C-rich stars defined by Aoki et al. (2007) (Fig. 3, empty circles).

In the MW halo a significant fraction of metal-poor stars, i.e., stars with $[Fe/H] \leq -2$, is enriched in carbon ($[C/Fe] > 0.7$ dex)⁶. The fraction of carbon enriched metal-poor (CEMP) stars seems to be function of decreasing metallicity (e.g. Beers & Christlieb 2005), suggesting that large amounts of carbon were synthesised in the early Universe when the oldest and most metal-poor stars formed.

Until very recently, despite extensive observational searches, only a few carbon-rich stars were known in dSphs, even at low metallicities. In Sextans one CEMP star has been identified with $[C/Fe] = +1$ by Honda et al. (2011) (star S15-19 from Aoki et al. (2009)), and one moderately enhanced carbon star with $[C/Fe] = +0.4$ by Tafelmeyer et al. (2010). A CEMP star has been also discovered in Draco (Cohen & Huang 2009) and Sculptor (Skúladóttir et al. 2015; Salvadori et al. 2015). Finally, Kirby et al. (2015) studied a sample of 398 giants in the Sculptor, Fornax, Ursa Minor, and Draco. They identified 11 very carbon-rich giants (eight previously known) in three dSphs (namely Fornax, Ursa Minor, and Draco).

Since the MW halo is expected to be at least partially composed of disrupted dSphs accreted by the Galactic halo, it is important to carefully compare the carbon-enhanced fraction of the MW stellar halo with the values observed in dSphs. The recent study of Chiti et al. (2018) at low resolution ($R \sim 2000$) found that CEMP stars at metallicities below $[Fe/H] < -3.0$ constitute 36% of the observed stars in Sculptor. The measured fraction is comparable to the fraction of 30% observed by Yong et al. (2013) in the Milky Way halo (Placco et al. 2014), suggesting that some stars now populating the Galactic halo may have originated from accreted early analogs of dwarf galaxies. More and higher resolution studies are needed to confirm such fractions inside the dwarf galaxies. Moreover, the identification of carbon-rich stars and comparisons between galaxies may well be revised in light of 3D-NLTE treatment at similar stellar evolutionary stage. Indeed Amarsi et al. (2019) have shown that, for main sequence stars, the rise in carbon overabundance with decreasing metallicity was vanishing. However, most our knowledge in dwarf galaxies comes from giant stars, hence the question of the impact of 3D-NLTE on C is still to be uncovered.

5.2. Sodium

Figure 4 presents the results of LTE calculations for $[Na/Fe]$ ratios as a function of metallicity in Sextans (this paper and Tafelmeyer et al. 2010), Sculptor (Jablonka et al. 2015), and Fornax (Tafelmeyer et al. 2010), compared to $[Na/Fe]$ abundances measured in MW halo stars. Similarly to the other dwarfs, Sextans is following the MW trend, with our stars on the upper envelope of the dispersion range. We do not consider here the Na abundances measured by Aoki et al. (2009) since they have been obtained from EQW measurements of two strong Na D features at 5889 and 5895 Å with EQW which typically exceed 100 mÅ (see § 5.3). However the Na doublet at 5889 and 5895 Å is also strongly affected by NLTE effects. According to the NLTE calculation by Lind et al. (2011)⁷, the NLTE corrections for the two Na lines are both negative.

⁶ Throughout this paper, we adopt the Aoki et al. (2007) criterion, to define carbon-enhanced objects

⁷ <http://www.inspect-stars.com/>

Table 4: Derived abundances for S04–130 and S11–97 and the Aoki 2009’s stars along with their associated errors (see § 3.3.1).

	Fe I	Fe II	C	Na I	Mg I	Al I	Si I	Ca I	Sc II	Ti I	Ti II	V II	Cr I	Mn I	Co I	Ni I	Zn I	Sr II	Y II	Zr II	Ba II
log($\epsilon(X)_{\odot}$)	7.50	7.50	8.43	6.24	7.60	6.45	7.51	6.34	3.15	4.95	4.95	3.93	5.64	5.43	4.99	6.22	4.56	2.87	2.21	2.58	2.18
S04-130																					
Nb lines*	42	5	1	2	5	2	–	9	7	11	19	1	7	5	4	4	1	2	2	1	4
log($\epsilon(X)$)	4.56	4.80	4.96	3.80	5.11	2.96	–	3.58	0.37	2.04	2.30	<0.95	2.53	2.21	2.05	3.40	2.25	0.06	<-1.16	<-0.25	-1.56
[X/H]	-2.94	-2.70	-3.47	-2.44	-2.49	-3.49	–	-2.76	-2.78	-2.91	-2.65	<-2.98	-3.11	-3.22	-2.94	-2.82	-2.31	-2.80	<-3.37	<-2.83	-3.74
[X/Fe]	–	+0.24	-0.53	+0.50	+0.45	-0.55	–	+0.18	+0.16	+0.03	+0.29	<-0.04	-0.17	-0.28	-0.00	+0.11	+0.63	+0.13	<-0.43	<+0.11	-0.80
Error	0.11	0.11	0.15	0.11	0.11	0.11	–	0.14	0.15	0.11	0.15	–	0.11	0.11	0.13	0.17	0.11	0.11	–	–	0.11
S11-97																					
Nb lines*	44	4	1	2	5	1	–	11	7	10	20	–	9	5	4	4	1	2	2	1	3
log($\epsilon(X)$)	4.49	4.54	4.87	3.79	5.08	3.05	–	3.59	0.37	1.97	2.26	–	2.52	2.07	1.78	3.37	2.10	-0.48	<-1.17	<-0.39	-1.61
[X/H]	-3.01	-2.96	-3.56	-2.45	-2.52	-3.40	–	-2.75	-2.78	-2.98	-2.69	–	-3.12	-3.36	-3.21	-2.85	-2.46	-3.34	<-3.38	<-2.97	-3.79
[X/Fe]	–	+0.05	-0.55	+0.56	+0.49	-0.39	–	+0.26	+0.23	+0.03	+0.32	–	-0.11	-0.35	-0.20	+0.16	+0.55	-0.34	<-0.37	<+0.04	-0.78
Error	0.11	0.27	0.16	0.11	0.11	0.11	–	0.11	0.13	0.11	0.13	–	0.16	0.11	0.11	0.18	0.11	0.18	–	–	0.11
S10-14																					
Nb lines*	30	4	–	–	1	–	–	1	–	–	2	–	2	–	–	–	–	–	–	–	1
log($\epsilon(X)$)	4.49	4.63	–	–	4.88	–	–	3.55	–	–	2.12	–	2.20	–	–	–	–	–	–	–	-1.72
[X/H]	-3.01	-2.87	–	–	-2.72	–	–	-2.79	–	–	-2.83	–	-3.44	–	–	–	–	–	–	–	-3.90
[X/Fe]	–	+0.15	–	–	+0.29	–	–	+0.22	–	–	+0.19	–	-0.43	–	–	–	–	–	–	–	-0.89
Error	0.19	0.38	–	–	0.20	–	–	0.20	–	–	0.18	–	0.38	–	–	–	–	–	–	–	0.18
S11-13																					
Nb lines*	25	2	–	–	1	–	–	2	1	1	1	–	2	–	–	1	–	–	–	–	2
log($\epsilon(X)$)	4.45	4.69	–	–	4.78	–	–	3.47	0.16	1.64	2.38	–	2.10	–	–	3.36	–	–	–	–	-1.65
[X/H]	-3.05	-2.81	–	–	-2.82	–	–	-2.87	-2.99	-3.31	-2.58	–	-3.53	–	–	-2.86	–	–	–	–	-3.83
[X/Fe]	–	+0.24	–	–	+0.23	–	–	+0.18	+0.06	-0.26	+0.48	–	-0.48	–	–	+0.19	–	–	–	–	-0.78
Error	0.20	0.20	–	–	0.20	–	–	0.20	0.20	0.20	0.20	–	0.20	–	–	0.20	–	–	–	–	0.20
S11-37																					
Nb lines*	26	3	–	–	1	–	–	2	1	1	2	–	2	–	–	1	–	–	–	–	2
log($\epsilon(X)$)	4.52	4.70	–	–	4.94	–	–	3.51	0.31	1.76	2.17	–	2.21	–	–	3.30	–	–	–	–	-1.68
[X/H]	-2.98	-2.80	–	–	-2.66	–	–	-2.83	-2.84	-3.19	-2.78	–	-3.43	–	–	-2.92	–	–	–	–	-3.86
[X/Fe]	–	+0.18	–	–	+0.32	–	–	+0.15	+0.14	-0.21	+0.20	–	-0.45	–	–	+0.06	–	–	–	–	-0.87
Error	0.18	0.18	–	–	0.20	–	–	0.16	0.20	0.20	0.69	–	0.19	–	–	0.19	–	–	–	–	0.30
S12-28																					
Nb lines*	35	5	–	–	2	–	–	3	3	2	5	–	1	1	–	–	–	–	–	–	2
log($\epsilon(X)$)	4.50	4.59	–	–	4.96	–	–	3.61	0.11	1.89	2.29	–	2.39	2.16	–	–	–	–	–	–	-1.06
[X/H]	-3.00	-2.91	–	–	-2.64	–	–	-2.73	-3.04	-3.06	-2.66	–	-3.25	-3.27	–	–	–	–	–	–	-3.24
[X/Fe]	–	+0.09	–	–	+0.36	–	–	+0.27	-0.04	-0.06	+0.34	–	-0.25	-0.27	–	–	–	–	–	–	-0.24
Error	0.18	0.19	–	–	0.16	–	–	0.16	0.19	0.17	0.17	–	0.20	0.22	–	–	–	–	–	–	0.17
S14-98																					
Nb lines*	17	1	–	–	1	–	–	3	1	1	4	–	2	–	–	–	–	–	–	–	2
log($\epsilon(X)$)	4.58	5.07	–	–	4.96	–	–	3.89	0.21	2.57	2.53	–	2.38	–	–	–	–	–	–	–	-1.63
[X/H]	-2.92	-2.43	–	–	-2.64	–	–	-2.45	-2.94	-2.38	-2.42	–	-3.26	–	–	–	–	–	–	–	-3.81
[X/Fe]	–	+0.49	–	–	+0.29	–	–	+0.47	-0.01	+0.54	+0.50	–	-0.33	–	–	–	–	–	–	–	-0.89
Error	0.17	0.20	–	–	0.20	–	–	0.23	0.21	0.20	0.48	–	0.18	–	–	–	–	–	–	–	0.31
S15-19																					
Nb lines*	22	3	–	–	2	–	–	5	1	1	9	–	2	–	–	1	–	1	–	–	2
log($\epsilon(X)$)	4.28	4.19	–	–	5.01	–	–	3.64	0.64	2.05	1.94	–	2.30	–	–	2.96	–	-1.27	–	–	-0.30
[X/H]	-3.22	-3.31	–	–	-2.59	–	–	-2.70	-2.51	-2.90	-3.01	–	-3.34	–	–	-3.26	–	-4.14	–	–	-2.48
[X/Fe]	–	-0.09	–	–	+0.63	–	–	+0.52	+0.71	+0.32	+0.21	–	-0.12	–	–	-0.04	–	-0.92	–	–	+0.74
Error	0.19	0.23	–	–	0.19	–	–	0.19	0.21	0.19	0.21	–	0.19	–	–	0.19	–	0.28	–	–	0.19

Notes. * Number of lines kept after a careful selection of the best fitted lines.

Mashonkina et al. (2017b) computed NLTE corrections for 59 very metal-poor stars in seven dSphs and the MW halo. At metallicity $[\text{Fe}/\text{H}] = -3$, the Na $\Delta[\text{NLTE-LTE}]$ are ranging from -0.2 to -0.4 dex, which seems to be in agreement with the Lind et al. (2011) computations. These orders of magnitude for the NLTE corrections are mentioned to provide an idea of where the stars would actually stand.

5.3. The α elements

The plateau at $[\alpha/\text{Fe}] \sim +0.4$ dex seen in the Milky Way metal-poor stellar population indicates that the ejecta from massive stars were sufficiently well mixed in the ISM. This is also the case for Sculptor, where the majority of stars follow the MW halo trend (e.g. Jablonka et al. 2015). Conversely, there are hints

that lower mass classical dSphs, such as Sextans and Carina, could have a larger dispersion at fixed metallicity. In the case of Carina this is expected because of its star formation history, characterized by at least three distinct bursts (Hurley-Keller et al. 1998; Santana et al. 2016) that are so far interpreted as resulting from interactions with the Milky Way (Fabrizio et al. 2011, 2016; Pasetto et al. 2011). In Sextans, the observed dispersion in $[\alpha/\text{Fe}]$, when data from Aoki et al. (2009) and Tafelmeyer et al. (2010) are considered, has been attributed to the effect of the smaller number of supernovae enriching the ISM from which the observed stars were born, and to the coexistence of pockets of ISM with various abundances.

In the newly discovered EMPs observed with UVES, we measure an over-abundance in $[\alpha/\text{Fe}] \sim +0.4$ dex (see Figure 6), which is comparable with the typical $[\alpha/\text{Fe}]$ value observed in

Table 5: Changes in the mean abundances $\Delta[X/H]$ caused by a 100 K increase in T_{eff} accompanied by a +0.1 dex increase in $\log(g)$ and a +0.15 km s⁻¹ on v_t increase in the microturbulence velocity for star S04-130.

X	$\delta\log\epsilon(X)$
Fe I	+0.12
Fe II	+0.05
C	+0.10
Na I	+0.25
Mg I	+0.07
Al I	+0.21
Ca I	+0.09
Sc II	+0.05
Ti I	+0.18
Ti II	+0.04
Cr I	+0.15
Mn I	+0.13
Co I	+0.12
Ni I	+0.13
Zn I	+0.03
Sr II	+0.15
Ba II	+0.07

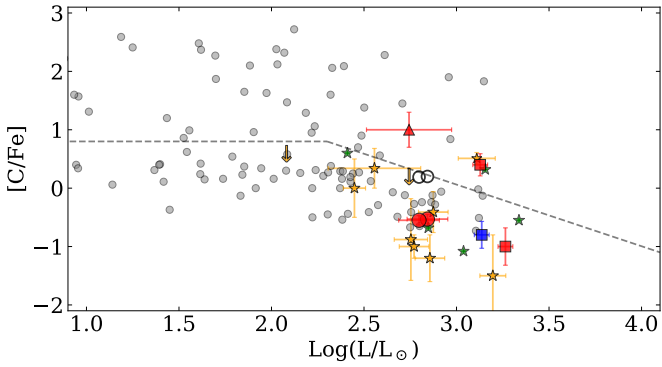


Fig. 3: $[C/Fe]$ as a function of $\log(L/L_{\text{sun}})$ for Galactic dwarf satellite and halo red giants with metallicities $[Fe/H] < -2.5$. The Sextans stars we analysed are represented by large red circles. Red squares are Sextans stars from Tafelmeyer et al. (2010), red triangle is the Sextans carbon-rich star from Honda et al. (2011). Grey dots denote the $[C/Fe]$ abundances of Milky Way halo stars from Yong et al. (2013). RGB stars in Sculptor (Jablonka et al. 2015; Simon et al. 2015; Tafelmeyer et al. 2010), Fornax (Tafelmeyer et al. 2010), and Draco (Shetrone et al. 2013; Cohen & Huang 2009) are shown in orange, blue, and green; respectively. The dotted line is the Aoki et al. (2007) dividing line for carbon enhancement, which takes into account the depletion of carbon with evolution along the RGB.

the halo of the Milky Way. This is in stark contrast with the result of Aoki et al. (2009), who obtained solar $[\alpha/Fe]$ ratios for the majority of their sample.

Therefore, in order to investigate into this apparent discrepancy, we re-analysed Aoki et al. (2009) stars following our methodology. There are some differences between the two analyses. First, Aoki et al. (2009) determined the stellar effective temperatures by adopting the $V - K$ colour index (combined with a colour-temperature calibration), while we derived our temperatures by minimizing the trend of Fe I abundances versus their

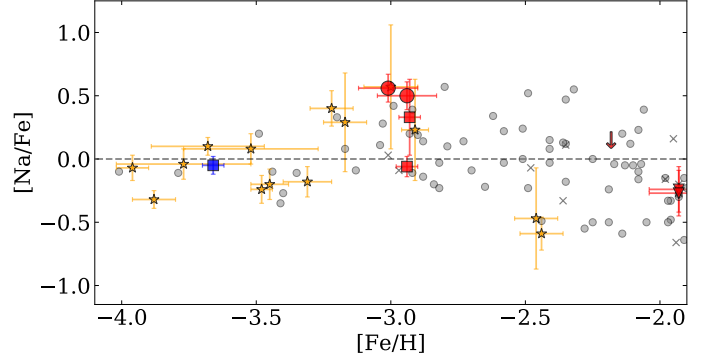


Fig. 4: Sodium-to-iron ratio as a function of $[Fe/H]$ are shown for metal-poor stars in Sextans, Sculptor, and Milky Way halo stars. Symbols are the same as in Fig. 6. Stars studied in this paper are the large red symbols.

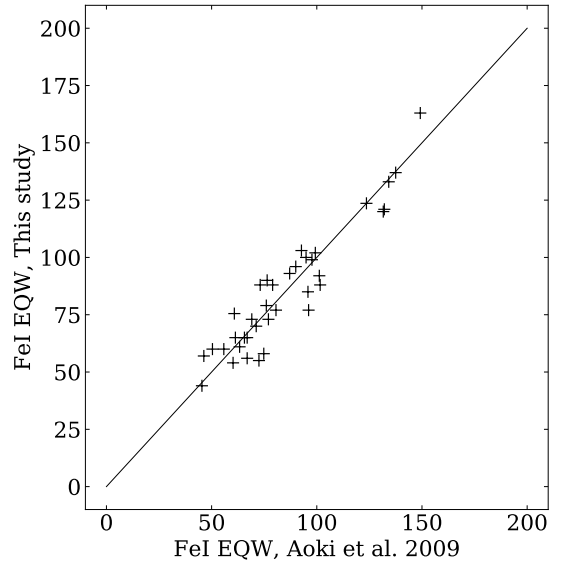


Fig. 5: Comparison for star S11-37 between Aoki et al. (2009) and the present analysis on the measured Fe I EQWs in common.

excitation potential (χ_{exc}). Second, we applied a different Gaussian fitting method to measure EQWs. Third, Aoki et al. (2009) used the Kurucz (1993) atmosphere models while we use the MARCS 1D spherical models.

We started by comparing our measured EQWs with those presented in Aoki et al. (2009). For that exercise, we considered the star S11-37, which is the one with the lowest metallicity in the group characterised the low α -element abundances. We retrieved the reduced spectra (8 exposures of 1800s for each, obtained in the blue and red arms of the Subaru High-Dispersion Spectrograph) from the JVO database⁸ and applied the same procedure as described in Sect. 2.2, with small adjustments to the HDS data. Briefly, the exposures were combined with IRAF, but the orders were extracted and fitted individually with DAOSPEC, in order to avoid any continuum modulation. Figure 5 shows that the EQWs measured using our approach are in excellent agreement with those listed in Aoki et al. (2009). Therefore, we decided to use Aoki et al. (2009) EQWs to re-derive abundances as described in §3.

⁸ <https://jvo.nao.ac.jp/portal/subaru/hds.do>

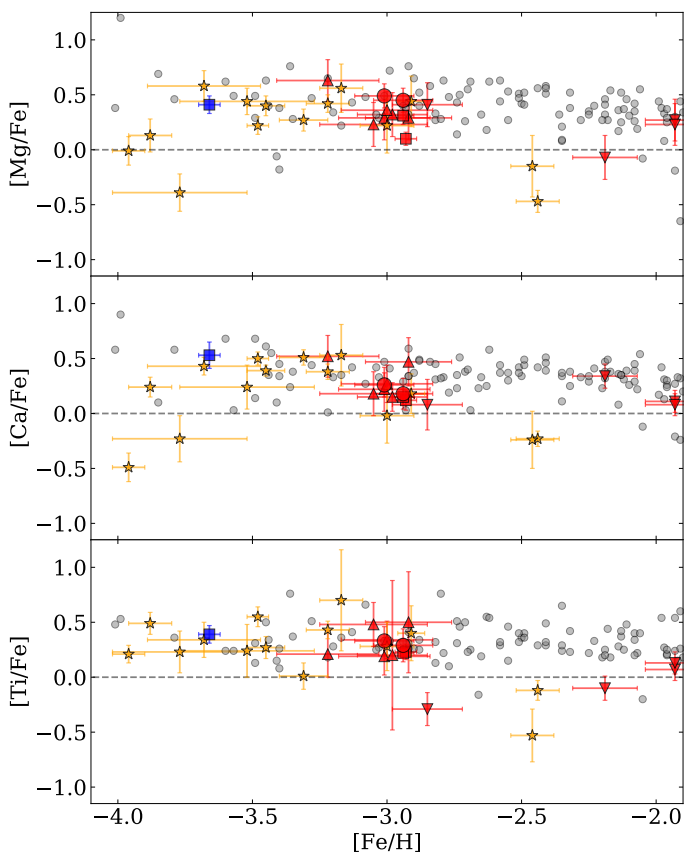


Fig. 6: Abundance ratios for the α elements Mg, Ca, and Ti (from top to bottom) as a function of $[\text{Fe}/\text{H}]$ are shown. Sextans stars are large red symbols. New EMP stars studied in this paper are the red circles. Sample of Aoki et al. (2009) re-analysed in this paper are the red triangles. Data from Shetrone et al. (2001b) are upside-down triangles. Grey dots are literature data for MW halo stars (Venn et al. 2004b; Cohen et al. 2013; Yong et al. 2013; Ishigaki et al. 2013). Orange and blue symbols refer to RGB stars observed in Sculptor (Jablonka et al. 2015; Tafelmeyer et al. 2010; Starkenburg et al. 2013; Simon et al. 2015) and Fornax (Tafelmeyer et al. 2010); respectively.

The star S15–19, with the lowest metallicity in the dataset of Aoki et al. (2009), has been re-observed and re-discussed by Honda et al. (2011) and has been confirmed to be a CEMP-s star. For the homogeneous reanalysis we use the new EQWs measured by Honda et al. (2011).

The abundances of many elements in Aoki et al. (2009) were obtained from classical EQWs analysis of strong lines which fall outside of our adopted criteria to select reliable lines. Our final atmospheric parameters and metallicities differ slightly, because of the different methodology between the two studies. We found a mean difference of -90K , -0.2 cgs , -0.7 km.s^{-1} and -0.2 dex , in T_{eff} , $\log(g)$, v_t , and $[\text{Fe}/\text{H}]$, respectively. Since the uncertainties on EQW measurements are not available, errors for the main abundances were computed from the standard deviation of individual line abundances. For the elements relying on a single line, we adopted the conservative error of 0.2 dex.

Figure 6 shows the measured abundances of α -elements from our newly observed EMPs and the re-analysis of Aoki et al. (2009) stars. The two Sextans stars presented in the previous paper of this series (Tafelmeyer et al. 2010) are also shown.

Sextans stars have $[\text{Mg}/\text{Fe}]$ abundance ratios that nicely follow the Galactic halo trend. Except for a single star with $[\text{Mg}/\text{Fe}] \sim -0.10$, we do not confirm the presence of a low- α population as claimed in Aoki et al. (2009). Stars with homogeneously derived abundances (e.g., large red symbols, triangles and squares in Fig. 6), appear also to be enhanced in Ti II at the level observed in Mg and Ca.

5.4. Iron-peak elements

Figure 7 presents the abundance ratios of scandium, nickel, cobalt, zinc, chromium and manganese as a function of metallicity. These elements are all produced by explosive nucleosynthesis.

The scandium abundances of our stars follow very closely the Milky Way halo trend. The Sc production is dominated by SNeII (e.g. Woosley et al. 2002; Battistini & Bensby 2015), thus the trend of Sc II/Fe with iron nicely follows the run of the α -elements with metallicity.

Ni and Co can be produced also by SNeIa (e.g. Travaglio et al. 2005; Kirby et al. 2018). However, the contribution by SNeIa starts dominating the chemical evolution of the galaxy at higher metallicities ($[\text{Fe}/\text{H}] \geq -2$; Theler et al. (2019)). Thus, the behaviour of Ni/Fe in the low metallicity range investigated here can be attributed to Ni production by complete and incomplete Si burning.

Co and Zn are produced by the complete Si burning when the peak temperature of the shock material is above $5 \times 10^9\text{ K}$ (Nomoto et al. 2013). The $[\text{Co}/\text{Fe}]$ ratios observed in our Sextans stars are covering the lower tail of the distribution in the Milky Way halo, similarly to the Fornax and three of the Sculptor EMPS. This could be simply an observational bias in our data sample since in dSphs we normally observe bright evolved RGB stars, which have lower temperatures and surface gravities than those in the MW halo. Additionally, these abundances should be corrected for the NLTE effect. These corrections depend on the stellar parameters as well (Bergemann et al. 2010; Kirby et al. 2018). It is interesting to note the lowest $[\text{Co}/\text{Fe}]$ EMPS in Sculptor are also the coolest, in the same temperature range $\sim 4500\text{K}$ as in Sextans (Starkenburg et al. 2013; Jablonka et al. 2015). The Fornax EMPS is even cooler ($\sim 4300\text{K}$, Tafelmeyer et al. 2010). Unfortunately, there is no NLTE corrections for the range of atmospheric parameters of our stars that would help shed light on the relative strength of the corrections.

The Zn abundances are measured from a weak line (with EQW of 23 to 30 mÅ) at 4810 Å. However, thanks to the relatively high (~ 50) S/N ratio of the spectra around the Zn feature, we were able to measure for the first time accurate Zn abundances at this very low metallicities in a classical dwarf galaxy. The measured Zn abundances perfectly follow the $[\text{Zn}/\text{Fe}]$ vs. $[\text{Fe}/\text{H}]$ observed in the MW very metal-poor stars, with an enhancement up to $\sim 0.7\text{ dex}$. The production sites of Zn remain uncertain, the increasing enhancement when metallicity is decreasing suggests that Zn was produced efficiently at the very early stages of the galaxies formation, likely in SNeII. But the production through classical SNeII was shown to be insufficient to explain the observed $[\text{Zn}/\text{Fe}]$ (Hirai et al. 2018; Tsujimoto & Nishimura 2018).

In the incomplete Si-burning region, the after-decay products include chromium and manganese (Nomoto et al. 2013). Figure 7 shows that the $[\text{Cr}/\text{Fe}]$ and $[\text{Mn}/\text{Fe}]$ trends with $[\text{Fe}/\text{H}]$ in Sextans stars well follows the Galactic one.

Bergemann & Cescutti (2010) have shown that in stars over the large range of metallicities between $-3.2 \leq [\text{Fe}/\text{H}] \leq -0.5$, the

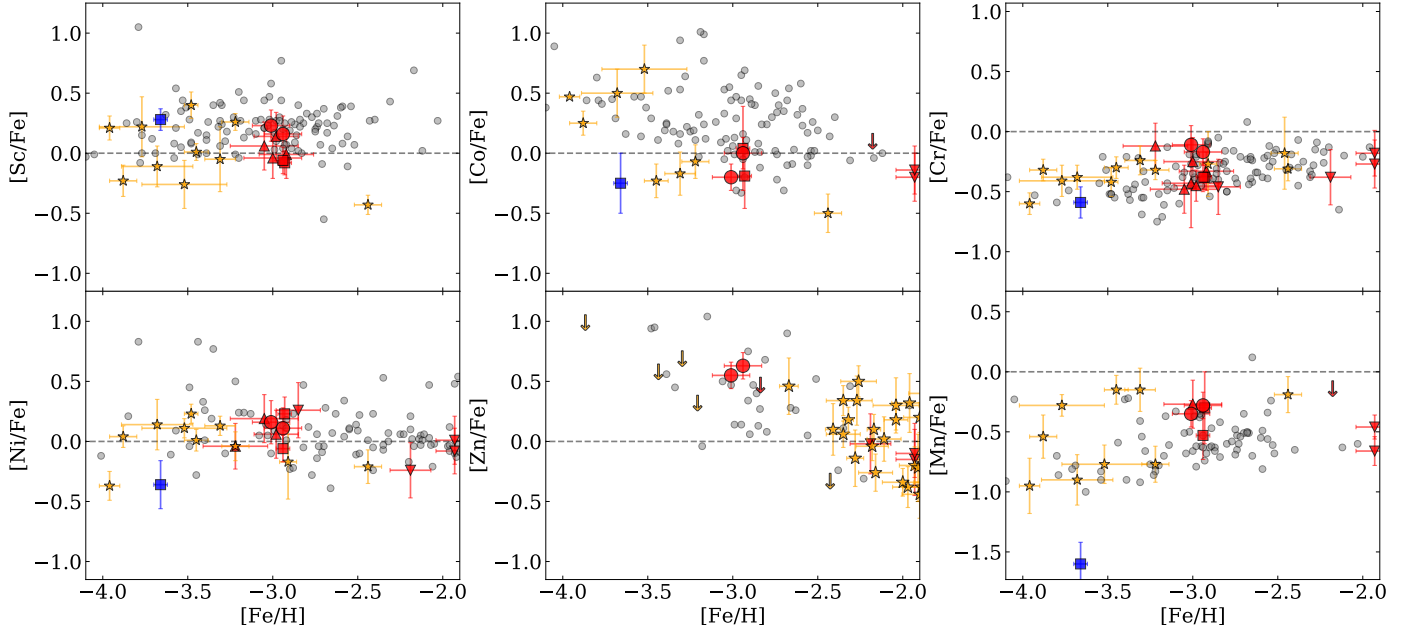


Fig. 7: From left to right, top to bottom: $[\text{Sc}/\text{Fe}]$, $[\text{Co}/\text{Fe}]$, $[\text{Cr}/\text{Fe}]$, $[\text{Ni}/\text{Fe}]$, $[\text{Zn}/\text{Fe}]$, and $[\text{Mn}/\text{Fe}]$ are shown for metal-poor stars in Sextans, Sculptor, Fornax, and Milky Way halo stars. Symbols are the same as in Fig. 6. Stars studied in this paper are the large red symbols.

$[\text{Cr}/\text{Fe}]$ ratio computed in NLTE is roughly solar, which is consistent with current views on the production of these iron peak elements in supernovae. Thus, the apparent increase of the $[\text{Cr}/\text{Fe}]$ ratios with metallicity in MW stars in Figure 7 is not real but rather due to the LTE approximation. NLTE corrections are not available for the range of stellar APs explored here. Nonetheless, NLTE corrections on Cr abundances are expected to be positive for bright giants (L. Mashonkina, *priv. comm.*).

5.5. Neutron capture elements

The heavy elements (heavier than Zn) are synthesized through two main processes. The s -process operates by slow neutron capture on seed nuclei on a long time scale (i.e., the neutron capture is slow compared to the β decay of the affected nucleus). The stellar sources for s -process production are asymptotic giant branch (AGB) stars (e.g. Busso et al. 1999; Käppler et al. 2011; Bisterzo et al. 2012). The r -process instead occurs on a very short time scale in violent events (e.g. Cameron 1957). High-entropy neutrino-driven winds of core-collapse supernovae (CCSNe) have traditionally been considered the sites of r -process nucleosynthesis (e.g. Sneden et al. 2008). However, they have been ruled out as responsible for the origin of the main r -process elements by observations and simulations (Wanajo 2013; Macias & Ramirez-Ruiz 2018) and other exotic types of CCSNe have been put forward (e.g., magnetorotational supernovae; Nishimura et al. 2015). The recent LIGO/Virgo discovery of gravitational waves from the neutron star merger (NSM) GW170817 (Abbott et al. 2017) and the follow-up kilonova observations (Pian et al. 2017) have shown that NSMs produce copious amount of r -process material (e.g. Lattimer & Schramm 1974; Freiburghaus et al. 1999; Côté et al. 2017). This notion is also supported by the detection of r -process enrichment in the ultra-faint dwarf (UFD) Reticulum II (Ji et al. 2016; Roederer et al. 2016). However, the evidence that r -process is found also in low mass systems where NSMs should be rare suggests that

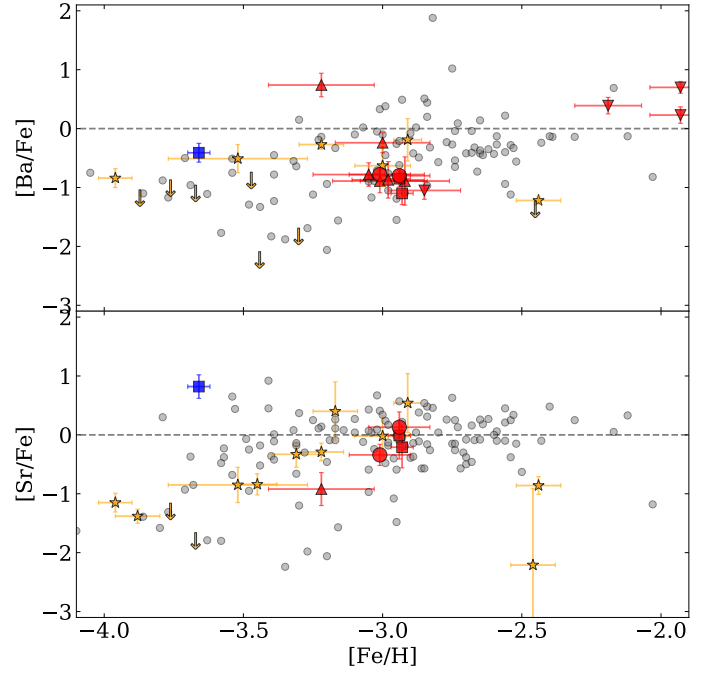


Fig. 8: Neutron-capture elements : Barium-to-iron ratio on top and strontium-to-iron ratio at the bottom, as a function of $[\text{Fe}/\text{H}]$ in Sextans seen in red, compared to the Milky Way Halo stars in grey. The large circles represent the new sample in Sextans. Orange symbols refer to Sculptor.

there could be different sites/conditions for the production of r -process elements (Travaglio et al. 2004; Jablonka et al. 2015; Mashonkina et al. 2017b; Hansen et al. 2018).

These two distinct processes produce generally different isotopes of a given heavy element, and different element ratios. Two

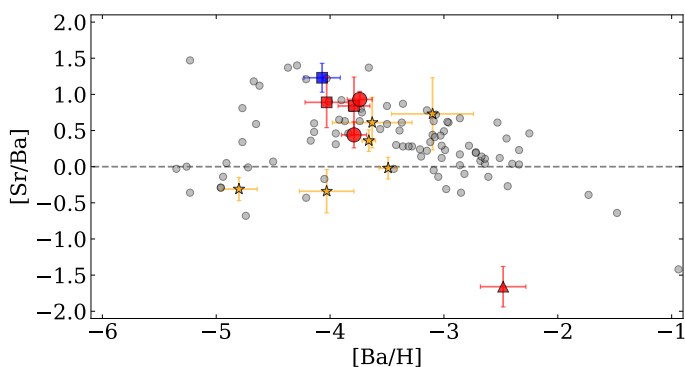


Fig. 9: Barium-to-strontium ratio as a function of $[Ba/H]$ in Sextans seen in red, compared to the Milky Way halo stars presented in grey. Sculptor is shown in orange, Fornax is in blue. References are in Figure 6.

neutron capture elements are measurable in our stars: barium and strontium. At very low metallicity (i.e. $[Fe/H] \leq -2.5$), a significant enrichment by AGBs is not expected, thus in our EMP stars, we expect a pure r -process origin for the neutron-capture elements.

Europium can be formed basically only through the r -process. However, Eu measurements in EMP stars are rare, since Eu lines are very weak at low-metallicities. We were not able to detect clean Eu features in our spectra. Nonetheless, $[Eu/Fe]$ seems to well correlate with $[Ba/Fe]$ for $[Fe/H]$ for metallicities $[Fe/H] \leq -2.5$ (e.g. Mashonkina et al. 2010; Spite & Spite 2014). Thus, at very low metallicity, even Ba has been formed by the r -process.

Sr and Ba abundances are shown in Figure 8 as a function of metallicity. As found earlier, $[Ba/Fe]$ is generally below solar in the EMP stars, with a significant scatter (Travaglio et al. 2004; François et al. 2007). In the same plot, we show also abundances for stars observed at high-resolution in the MW halo, Fornax, and Sculptor (see Fig. 6 for full references). In the MW halo sample a large dispersion in both $[Sr/Fe]$ and $[Ba/Fe]$ can be observed at metallicities lower than $[Fe/H] \leq -2.8$ and -2.5 for Sr and Ba; respectively (e.g. Andrievsky et al. 2009, 2010; Hansen et al. 2013; Mashonkina et al. 2017b). Above this metallicity, $[Sr/Fe]$ and $[Ba/Fe]$ become steadily solar and their dispersion is largely diminished.

Figure 8 shows that, except for S15-19, which is a carbon-rich star with evidence for s -process enrichment (Honda et al. 2011), all Sextans EMPS so far investigated at very high resolution have sub-solar $[Ba/Fe]$ ratios at $[Fe/H] \sim -3$, to a level which is close to the one encountered at much lower metallicities for Fornax and Sculptor and in the ultra-faint dwarfs (Simon 2019), hence tracing the initial trend between Fe and Ba, most likely arising from core-collapse supernovae. This concentration is most likely a coincidence, since at higher metallicities $[Ba/Fe]$ reaches the solar plateau. It is anyway useful to appreciate the difference in Sr and Ba behaviors. For the same stars, $[Sr/Fe]$ is clumped around the solar value in a similar way as the Milky Way halo population, suggesting similar enrichment processes for strontium.

Figure 9 shows the run of the $[Sr/Ba]$ ratio plotted against $[Ba/H]$. If Ba and Sr were formed by the same process, their ratio should not vary with $[Ba/H]$. All Sextans stars observed at high resolution so far are perfectly located at the top of the decreasing branch of $[Sr/Ba]$ with $[Ba/H]$, providing confirmation that the source responsible for the production of lighter (Sr) neutron

capture elements is at work at earlier times with respect to the processes responsible for the production of heavier (Ba) neutron capture elements (e.g. François et al. 2007; Mashonkina et al. 2017b; Spite et al. 2018; Frebel 2018; Hansen et al. 2018).

6. Summary

We have presented the analysis of high-resolution spectra of two metal-poor stars in the dwarf spheroidal galaxy Sextans, including the abundance derivation of 18 chemical elements. In particular, we provide the first measurements of Zn in a classical dSph in this metallicity range. These stars are confirmed as some of the most metal-poor stars known in Sextans. Literature spectra originally presented in Aoki et al. (2009) have been re-investigated in an homogeneous manner and abundances for Fe I, Fe II, Mg, Ca, Sc II, Ti I, Ti II, Cr, and Ba II re-derived. This full sample significantly increases the number of stars in the low metallicity range and gives new clues on the formation of Sextans. In particular, we demonstrate that the Sextans metal-poor population follows the Milky-Way halo-like plateau at $[\alpha/Fe] \sim 0.4$ with a normal scatter, contrary to previous results.

Most of the iron-peak elements are aligned with the MW halo distribution. Only cobalt is slightly depleted. We suggest on observational ground that $[Co/Fe]$ can scale with the stellar effective temperature and that differential NLTE corrections would put the Milky Way and dSph populations on the same scale.

The four Sextans (non carbon rich) EMPS analysed at high resolution have $[Fe/H] \sim -3$ and $[Ba/Fe] \sim -1$. This corresponds to the Ba floor seen at $[Fe/H]$ below -3.5 in the MW halo, in the UFDs and in Sculptor. At this metallicity and this Ba enrichment, $[Sr/Fe]$ is already solar providing confirmation that the source responsible for the production of the light neutron capture elements precedes the production of the heavier ones. It also shows that this source is already efficient at the galaxy mass of Sextans.

Acknowledgements. The authors warmly thank Lyudmila Mashonkina for useful discussions on the NLTE corrections. The authors acknowledge the support and funding of the International Space Science Institute (ISSI) through the International Team "Pristine". CL acknowledges financial support from the Swiss National Science Foundation (Ambizione grant PZ00P2_168065). GB acknowledges financial support through the grant (AEI/FEDER, UE) AYA2017-89076-P, as well as by the Ministerio de Ciencia, Innovación y Universidades (MCIU), through the State Budget and by the Consejería de Economía, Industria, Comercio y Conocimiento of the Canary Islands Autonomous Community, through the Regional Budget.

References

- Abbott, B. P., Abbott, R., Abbott, T. D., et al. 2017, Phys. Rev. Lett., 119, 161101
 Alonso, A., Arribas, S., & Martínez-Roger, C. 1999, A&AS, 140, 261
 Alvarez, R. & Plez, B. 1998, A&A, 330, 1109
 Amarsi, A. M., Nissen, P. E., Asplund, M., Lind, K., & Barklem, P. S. 2019, A&A, 622, L4
 Andrievsky, S. M., Spite, M., Korotin, S. A., et al. 2010, A&A, 509, A88
 Andrievsky, S. M., Spite, M., Korotin, S. A., et al. 2009, A&A, 494, 1083
 Aoki, W., Arimoto, N., Sadakane, K., et al. 2009, A&A, 502, 569
 Aoki, W., Beers, T. C., Christlieb, N., et al. 2007, ApJ, 655, 492
 Asplund, M., Grevesse, N., Sauval, A. J., & Scott, P. 2009, ARA&A, 47, 481
 Battaglia, G., Tolstoy, E., Helmi, A., et al. 2011, VizieR Online Data Catalog, 741
 Battistini, C. & Bensby, T. 2015, A&A, 577, A9
 Beers, T. C. & Christlieb, N. 2005, ARA&A, 43, 531
 Bergemann, M. & Cescutti, G. 2010, A&A, 522, A9
 Bergemann, M., Pickering, J. C., & Gehren, T. 2010, MNRAS, 401, 1334
 Bettinelli, M., Hidalgo, S. L., Cassisi, S., Aparicio, A., & Piotto, G. 2018, MNRAS, 476, 71
 Bisterzo, S., Gallino, R., Straniero, O., Cristallo, S., & Käppeler, F. 2012, MNRAS, 422, 849
 Breddels, M. A. & Helmi, A. 2013, A&A, 558, A35

- Busso, M., Gallino, R., & Wasserburg, G. J. 1999, *ARA&A*, 37, 239
- Cameron, A. G. W. 1957, *AJ*, 62, 9
- Cardelli, J. A., Clayton, G. C., & Mathis, J. S. 1989, *ApJ*, 345, 245
- Chiti, A., Simon, J. D., Frebel, A., et al. 2018, *ApJ*, 856, 142
- Cicuéndez, L. & Battaglia, G. 2018, *MNRAS*, 480, 251
- Cicuéndez, L., Battaglia, G., Irwin, M., et al. 2018, *A&A*, 609, A53
- Cohen, J. G., Christlieb, N., Thompson, I., et al. 2013, *ApJ*, 778, 56
- Cohen, J. G. & Huang, W. 2009, *ApJ*, 701, 1053
- Côté, B., Belczynski, K., Fryer, C. L., et al. 2017, *ApJ*, 836, 230
- Dekker, H., D'Odorico, S., Kaufer, A., Delabre, B., & Kotzłowski, H. 2000, in *Society of Photo-Optical Instrumentation Engineers (SPIE) Conference Series*, Vol. 4008, Proc. SPIE, ed. M. Iye & A. F. Moorwood, 534–545
- Fabrizio, M., Bono, G., Nonino, M., et al. 2016, *ApJ*, 830, 126
- Fabrizio, M., Nonino, M., Bono, G., et al. 2011, *PASP*, 123, 384
- François, P., Depagne, E., Hill, V., et al. 2007, *A&A*, 476, 935
- Frebel, A. 2018, *Annual Review of Nuclear and Particle Science*, 68, 237
- Frebel, A. & Norris, J. E. 2015, *ARA&A*, 53, 631
- Freiburghaus, C., Rosswog, S., & Thielemann, F. K. 1999, *ApJ*, 525, L121
- Gustafsson, B., Edvardsson, B., Eriksson, K., et al. 2008, *A&A*, 486, 951
- Hansen, C. J., Bergemann, M., Cescutti, G., et al. 2013, *A&A*, 551, A57
- Hansen, T. T., Holmbeck, E. M., Beers, T. C., et al. 2018, *ApJ*, 858, 92
- Hill, V., Skúladóttir, Á., Tolstoy, E., et al. 2019, *A&A*, 626, A15
- Hirai, Y., Saitoh, T. R., Ishimaru, Y., & Wanajo, S. 2018, *ApJ*, 855, 63
- Honda, S., Aoki, W., Arimoto, N., & Sadakane, K. 2011, *PASJ*, 63, 523
- Hurley-Keller, D., Mateo, M., & Nemeč, J. 1998, *AJ*, 115, 1840
- Irwin, M. & Hatzidimitriou, D. 1995, *MNRAS*, 277, 1354
- Irwin, M. J., Bunclark, P. S., Bridgeland, M. T., & McMahon, R. G. 1990, *MNRAS*, 244, 16P
- Ishigaki, M. N., Aoki, W., & Chiba, M. 2013, *ApJ*, 771, 67
- Jablonka, P., North, P., Mashonkina, L., et al. 2015, *A&A*, 583, A67
- Ji, A. P., Frebel, A., Chiti, A., & Simon, J. D. 2016, *Nature*, 531, 610
- Käppeler, F., Gallino, R., Bisterzo, S., & Aoki, W. 2011, *Reviews of Modern Physics*, 83, 157
- Karachentsev, I. D., Karachentseva, V. E., Huchtmeier, W. K., & Makarov, D. I. 2004, *AJ*, 127, 2031
- Kirby, E. N. & Cohen, J. G. 2012, *AJ*, 144, 168
- Kirby, E. N., Guo, M., Zhang, A. J., et al. 2015, *ApJ*, 801, 125
- Kirby, E. N., Xie, J. L., Guo, R., Kovalev, M., & Bergemann, M. 2018, *ApJS*, 237, 18
- Kupka, F., Piskunov, N., Ryabchikova, T. A., Stempels, H. C., & Weiss, W. W. 1999, *A&AS*, 138, 119
- Kupka, F. G., Ryabchikova, T. A., Piskunov, N. E., Stempels, H. C., & Weiss, W. W. 2000, *Baltic Astronomy*, 9, 590
- Kurucz, R. L. 1993, in *Astronomical Society of the Pacific Conference Series*, Vol. 44, IAU Colloq. 138: Peculiar versus Normal Phenomena in A-type and Related Stars, ed. M. M. Dworetsky, F. Castelli, & R. Faraggiana, 87
- Lattimer, J. M. & Schramm, D. N. 1974, *ApJ*, 192, L145
- Lee, M. G., Park, H. S., Park, J.-H., et al. 2003, *AJ*, 126, 2840
- Lee, M. G., Yuk, I.-S., Park, H. S., Harris, J., & Zaritsky, D. 2009, *ApJ*, 703, 692
- Letarte, B., Hill, V., Tolstoy, E., et al. 2010, *A&A*, 523, A17
- Lind, K., Asplund, M., Barklem, P. S., & Belyaev, A. K. 2011, *A&A*, 528, A103
- Łokas, E. L. 2009, *MNRAS*, 394, L102
- Macias, P. & Ramirez-Ruiz, E. 2018, *ApJ*, 860, 89
- Magain, P. 1984, *A&A*, 134, 189
- Mashonkina, L., Christlieb, N., Barklem, P. S., et al. 2010, *A&A*, 516, A46
- Mashonkina, L., Jablonka, P., Pakhomov, Y., Sitnova, T., & North, P. 2017a, *A&A*, 604, A129
- Mashonkina, L., Jablonka, P., Sitnova, T., Pakhomov, Y., & North, P. 2017b, *A&A*, 608, A89
- Mateo, M., Fischer, P., & Krzemiński, W. 1995, *AJ*, 110, 2166
- Nishimura, N., Takiwaki, T., & Thielemann, F.-K. 2015, *ApJ*, 810, 109
- Noguchi, K., Aoki, W., Kawonomoto, S., et al. 2002, *PASJ*, 54, 855
- Nomoto, K., Kobayashi, C., & Tominaga, N. 2013, *Annual Review of Astronomy and Astrophysics*, 51, 457
- North, P., Cescutti, G., Jablonka, P., et al. 2012, *A&A*, 541, A45
- Okamoto, S., Arimoto, N., Tolstoy, E., et al. 2017, *MNRAS*, 467, 208
- Pasetto, S., Grebel, E. K., Berczik, P., Chiosi, C., & Spurzem, R. 2011, *A&A*, 525, A99
- Pian, E., D'Avanzo, P., Benetti, S., et al. 2017, *Nature*, 551, 67
- Piskunov, N. E., Kupka, F., Ryabchikova, T. A., Weiss, W. W., & Jeffery, C. S. 1995, *A&AS*, 112, 525
- Placco, V. M., Frebel, A., Beers, T. C., & Stancliffe, R. J. 2014, *ApJ*, 797, 21
- Plez, B. 2012, *Turbospectrum: Code for spectral synthesis*, *Astrophysics Source Code Library*
- Press, W. H. & Schechter, P. 1974, *ApJ*, 187, 425
- Ramírez, I. & Meléndez, J. 2005, *ApJ*, 626, 465
- Roederer, I. U., Mateo, M., Bailey, John I., I., et al. 2016, *AJ*, 151, 82
- Ryabchikova, T. A., Piskunov, N. E., Kupka, F., & Weiss, W. W. 1997, *Baltic Astronomy*, 6, 244
- Salvadori, S., Skúladóttir, Á., & Tolstoy, E. 2015, *MNRAS*, 454, 1320
- Santana, F. A., Muñoz, R. R., de Boer, T. J. L., et al. 2016, *ApJ*, 829, 86
- Shetrone, M. D., Côté, P., & Sargent, W. L. W. 2001a, *ApJ*, 548, 592
- Shetrone, M. D., Côté, P., & Sargent, W. L. W. 2001b, *ApJ*, 548, 592
- Shetrone, M. D., Smith, G. H., Stanford, L. M., Siegel, M. H., & Bond, H. E. 2013, *AJ*, 145, 123
- Simon, J. D. 2019, *ARA&A*, 57, 375
- Simon, J. D., Jacobson, H. R., Frebel, A., et al. 2015, *ApJ*, 802, 93
- Skúladóttir, Á., Tolstoy, E., Salvadori, S., et al. 2015, *A&A*, 574, A129
- Snedden, C., Cowan, J. J., & Gallino, R. 2008, *ARA&A*, 46, 241
- Spite, F., Spite, M., Barbuy, B., et al. 2018, *A&A*, 611, A30
- Spite, M. & Spite, F. 2014, *Astronomische Nachrichten*, 335, 65
- Springel, V., Frenk, C. S., & White, S. D. M. 2006, *Nature*, 440, 1137
- Starkenburger, E., Hill, V., Tolstoy, E., et al. 2013, *A&A*, 549, A88
- Starkenburger, E., Hill, V., Tolstoy, E., et al. 2010, *A&A*, 513, A34
- Stetson, P. B. & Pancino, E. 2008, *PASP*, 120, 1332
- Tafelmeyer, M., Jablonka, P., Hill, V., et al. 2010, *A&A*, 524, A58
- Theler, R., Jablonka, P., Lardo, C., et al. 2019, *arXiv e-prints*, [arXiv:1911.08627](https://arxiv.org/abs/1911.08627)
- Tolstoy, E., Hill, V., & Tosi, M. 2009, *ARA&A*, 47, 371
- Travaglio, C., Gallino, R., Arnone, E., et al. 2004, *ApJ*, 601, 864
- Travaglio, C., Hillebrandt, W., & Reinecke, M. 2005, *A&A*, 443, 1007
- Tsujimoto, T. & Nishimura, N. 2018, *ApJ*, 863, L27
- Van der Swaelmen, M., Hill, V., Primas, F., & Cole, A. A. 2013, *A&A*, 560, A44
- Venn, K. A., Irwin, M., Shetrone, M. D., et al. 2004a, *AJ*, 128, 1177
- Venn, K. A., Irwin, M., Shetrone, M. D., et al. 2004b, *AJ*, 128, 1177
- Walker, M. G., McGaugh, S. S., Mateo, M., Olszewski, E. W., & Kuzio de Naray, R. 2010, *ApJ*, 717, L87
- Wanajo, S. 2013, *ApJ*, 770, L22
- White, S. D. M. & Rees, M. J. 1978, *MNRAS*, 183, 341
- Woosley, S. E., Heger, A., & Weaver, T. A. 2002, *Reviews of Modern Physics*, 74, 1015
- Yong, D., Norris, J. E., Bessell, M. S., et al. 2013, *ApJ*, 762, 26